Nonlinear Antenna Technology

BRIAN K. MEADOWS, TED H. HEATH, JOSEPH D. NEFF, EDGAR A. BROWN,
DAVID W. FOGLIATTI, MICHAEL GABBAY, VISARATH IN, PAUL HASLER, MEMBER, IEEE,
STEPHEN P. DEWEERTH, MEMBER, IEEE, AND WILLIAM L. DITTO

Invited Paper

Nonlinear antennas combine advances in nonlinear dynamics, active antenna design, and analog microelectronics to generate beam steering and beam forming across an array of nonlinear oscillators. Nonlinear antennas exploit two phenomena typically shunned in traditional designs: nonlinear unit cells and interelement coupling. The design stems from nonlinear coupled differential equation analysis that by virtue of the dynamic control is far less complex than the linear counterparts by eliminating the need for phase shifters and beam forming computers. These advantages arise from incorporating nonlinear dynamics rather than limiting the system to linear quasisteady state operation. A theoretical framework describing beam shaping and beam forming by exploiting the phase, amplitude, and coupling dynamics of nonlinear oscillator arrays is presented. Experimental demonstration of nonlinear beam steering is realized using analog microelectronics.

Keywords—Active antenna, analog VLSI, beam forming, beam steering, coupled oscillator array, nonidentical oscillators, nonlinear dynamics.

I. INTRODUCTION

Nonlinear antenna technology relies on array processing at microwave and millimeter-wave frequencies [1]. Active antenna design employs diodes, transistors, or nonlinear circuits distributed over a plane surface that interact with the free-space beams at the plane of radiation collection. Active antennas differ fundamentally from the passive antenna in two ways: the unit cells are nonlinear, and signal processing (dynamic interactions between cells) is done via mutual coupling. In passive antenna arrays, which employ some type of multipole as the unit cell, prescribing the geometry of the array controls the radiation pattern. Traditional array antenna design has not devoted significant effort toward deliberately controlling the mutual coupling between radiators.

Active antennas are inherently nonlinear dynamic systems that can generate a number of unusual nonlinear phenomena [2]–[4]. Over the last several years, an explosion of new analysis and control techniques for manipulating nonlinear dynamics has emerged [5]. New nonlinear techniques are especially well suited for active antenna design. Current array design practice strives to suppress any interelement coupling while minimizing noise [6]. However, the interplay between coupling and noise can be "tuned" to achieve optimal performance. This is done in a variety of ways in nonlinear devices by adjusting the coupling strength, changing the number of elements in the array, dynamically controlling the device potential, introducing spatial disorder into the array, or optimizing the input noise. These nontraditional design approaches have already been experimentally verified in prototype antennas.

Generically, any active antenna design is an ensemble of coupled nonlinear devices. The dynamics of coupled nonlinear arrays has been the subject of intense study in the last decade, particularly superconducting oscillator arrays [7], [8]. Fortuitously, the equation that governs the motion of exotic superconducting oscillators also describes the analog phase-locked loop (PLL) [9], one of the building blocks in active antennas. Therefore, advances in understanding the dynamics of superconducting oscillator arrays transfer to active antenna design. Of particular promise is the role of temporal and spatial fluctuations in synchronizing oscillator arrays.

During the past decade, insight into the dynamics of coupled nonlinear systems has produced a number of useful architectures. This work has shown that nonlinear arrays offer simple methods for phase control among array elements and hence beam scanning capability. Numerous X-band antenna experiments verify the theory and have demonstrated the practicality of the techniques [10]. A key experimental result demonstrates that exploiting mutual coupling can substantially reduce the physical size of an antenna [11].

Using coupled nonlinear elements is a radical departure from traditional antenna design, but the performance goals remain the same: high antenna gain, excellent control over the beam shape, and fast sweep-time of the array.

II. DYNAMICS OF DISORDER

When a collection of limit cycle oscillators is coupled to its nearest neighbor, frequency-locking between oscillators can occur. A phase gradient can be created across the chain by tuning the free-running frequencies of the boundary elements. Nearest-neighbor interactions transmit the change in phase across the array, forming a constant gradient that allows control over the propagation of the wave front (see Fig. 1). Areas in which this could play an important role are sensor arrays, beam steering, and beam-forming problems. As a first step toward applying these results to the beam steering problem, a one-dimensional (1-D) chain of analog PLLs is simulated. The PLLs are linearly coupled to their nearest neighbors and each element receives the globally applied signal $A\sin(\omega_D t)$ [12]. The equation of motion is

$$\ddot{\theta}_n + \gamma\dot{\theta}_n \cos\theta_n = -\omega_{0n}^2 \sin\theta_n$$
$$+ A\sin(\omega_D t) + \kappa(\theta_{n+1} + \theta_{n-1} - 2\theta_n) \quad (1)$$

where θ_n is the phase error of the nth PLL in the chain, ω_{0n} is the natural frequency of the nth PLL, and ω_D is the frequency of the global ac driving signal. The over-dot notation represents a derivative with respect to time. Spatial disorder is introduced through variations in the natural frequency ω_0 of each PLL. When all the elements are identical ($\Delta\omega_0 = 0$) the resulting motion is chaotic, i.e., no long-term frequency or phase coherence. If spatial disorganization is introduced into an array, then ordered motion emerges. The center and bottom panels demonstrate different schemes for spatial variation. While random spatial disorder produces periodic motion, the highest degree of coherence occurs when every other element in the array is spatially disordered.[1] Previous experiments by York and coworkers employing a chain of microwave oscillators provide evidence that spatial disorder does indeed control the phase matching between elements.

Fig. 1. Time evolution (horizontal) of a chain of 64 locally coupled analog PLLs, demonstrating how tuning spatial disorder can improve frequency and phase locking. Blue and red colors code angular velocities of the spatiotemporal evolution of array. In (a), the array of identical oscillators evolve with chaotic motion. Panel (b) illustrates the effect of randomly changing the natural frequency of every PLL in the chain by upwards of 20%. This converts the motion from chaotic to periodic (period 2), but with a large phase dispersion. Finally, sequence (c) illustrates the effect of disordering every other element by 50% ($\Delta\omega_0 = 0.5$). This results in periodic motion, but the phase dispersion is much sharper than in the previous case. The parameters used in the figure are $\gamma = 0.75$, $A = 0.4$, $\omega_0 = 1.0$, $\omega_D = 0.2$, and $\kappa = 0.5$.

III. THEORY OF NONLINEAR ANTENNA DYNAMICS

In this section a model of a 1-D coupled, nonlinear oscillator array is introduced. Later sections describe how to adjust various system parameters for beam shaping and beam steering.

The system under consideration [Fig. 2(a) and (b)] is a 1-D chain of voltage-controlled oscillators, each driving a separate patch antenna. Dominant interactions are taken to occur between neighboring elements, either through radiative or transmission line coupling, i.e., nearest-neighbor coupling is assumed.

Equations describing the amplitude and phase dynamics of the array elements are given by (2) and (3) [13]–[15]

$$\dot{A}_j = (p_j - A_j^2)A_j + kA_{j+1}\cos(\phi_{j+1} - \phi_j + \Phi)$$
$$+ kA_{j-1}\cos(\phi_{j-1} - \phi_j + \Phi) \quad (2)$$
$$\dot{\phi}_j = \omega_j + k\left(\frac{A_{j+1}}{A_j}\right)\sin(\phi_{j+1} - \phi_j + \Phi)$$
$$+ k\left(\frac{A_{j-1}}{A_j}\right)\sin(\phi_{j-1} - \phi_j + \Phi) \quad (3)$$

where ω_j is the natural frequency of the jth element, k and Φ are the coupling strength and coupling phase, respectively. As the periphery elements only possess a single nearest neighbor, the boundary conditions are given by $A_0 = A_{N+1} = 0$. Extending this model to encompass two-dimensional (2-D) rectangular arrays is relatively straightforward: a typical element would then be influenced by its four nearest neighbors, leading to four, rather than two, coupling terms.

This model possesses four parameters which may be used to control the array's dynamics: 1) the coupling strength k; 2) the coupling phase Φ; 3) the oscillator natural frequencies ω_j; and 4) the oscillator amplitude parameters p_j. The p_j and

---

[1]A fascinating analogy to nonidentical oscillator tuning occurs by introducing temporal disorder, rather than spatial disorder. The dynamical properties of nonlinear oscillator arrays driven by weak deterministic signals and noise constitute an active area of research. The interested reader should consult A. R. Bulsara, L. Gammaitoni "Tuning in to Noise," *Physics Today*, p. 39, March 1996, for an excellent introduction to noise induced coherence.
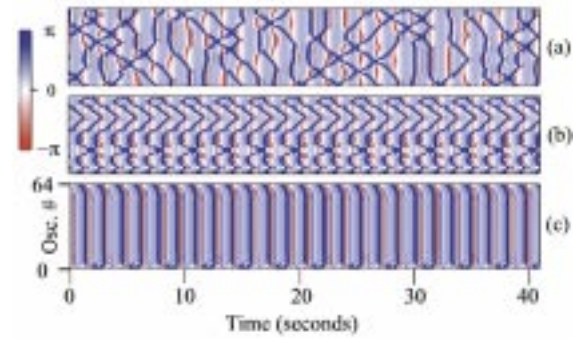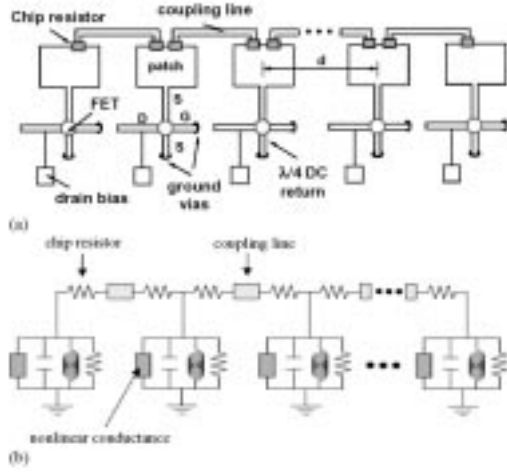
Fig. 2. (a) Nonlinear active antenna producing beam steering without phase shifters. The array is composed of voltage-controlled oscillators (VCOs) tied to simple patch radiators. Each active element is electrically coupled via a strip-line to a nearest neighbor in the array. By adjusting the varactor bias, the free running frequency of each oscillator can be altered. Beam steering is accomplished by changing the bias on the two boundary elements only. (b) Equivalent circuit schematic of a 1-D array of nonlinear oscillators with transmission-line coupling. The light gray box in the coupling line represents, in general, some form of RLC network. Although a parallel RLC combination in the oscillators has been assumed here, a series RLC has been shown to lead to a similar set of dynamical equations.

ω_j define the oscillator amplitude and frequency in the absence of coupling ($k = 0$).

A. The Phase Model

Unless otherwise stated, the following two simplifying assumptions will be invoked: the amplitude dynamics evolve on a much faster time scale than the phase dynamics and the oscillator amplitudes all rapidly settle down to a common value, i.e., $A_j \rightarrow a$. Thus, having specified the amplitudes, the oscillators will be described solely by their phases

$$\dot{\phi}_j = \omega_j + k[\sin(\phi_{j+1} - \phi_j + \Phi) + \sin(\phi_{j-1} - \phi_j + \Phi)] \quad (4)$$

where the boundary conditions become

$$\phi_0 = \phi_1 - \Phi \quad (5a)$$
$$\phi_{N+1} = \phi_N - \Phi. \quad (5b)$$

Moreover, note that the assumption of identical amplitudes effectively decouples the phase dynamics from the amplitude dynamics. Equation (4) will be referred to as the "phase model." Interestingly, similar equations have arisen in models of solid-state laser arrays, Josephson junction arrays, and PLL arrays as well as biological systems such as eel locomotion and the synchronized flashing of fireflies [16]–[21].

Whether dealing with the phase model or the full equations, the following sections of theoretical analysis share a common two-step approach. First, establish the existence of the solutions by substituting the desired solutions into the dynamical equations. From that, determine how the accessible parameters should be adjusted. Second, establish under what conditions those solutions are stable, i.e., physically realizable states of the coupled oscillator array.

For beam steering, one seeks to establish a spatially uniform phase gradient across the array; in other words, the elements should be phase-locked such that the phase difference between neighboring oscillators has the same value throughout the array. Mathematical solutions to the phase model are sought having the following form:

$$\phi_j = (j-1)\theta + \omega t. \quad (6)$$

In order for this to be a solution of the phase model equations, the natural frequencies must satisfy the following relations:

$$\omega_1 = \omega + k\sin(\theta + \Phi) \quad (7a)$$
$$\omega_j = \omega + (j-1)\dot{\theta} \quad (7b)$$
$$\omega_N = \omega + (N-1)\dot{\theta} - k\sin(\theta - \Phi). \quad (7c)$$

In the case of "static" ($\dot{\theta} = 0$) beam steering, i.e., when the main beam should point in a fixed direction, these conditions imply that the natural frequencies of only the two end elements need to be manipulated. In essence, two dc bias voltages have replaced N phase shifters. Alternatively, continuously scanning the beam ($\dot{\theta} \neq 0$) requires adjusting every oscillator's natural frequency in a time-dependent manner. This still proves advantageous, as a simple dc control network replaces the complex RF phase-control circuitry.

Having established the existence of the desired solutions, the question of their stability must now be considered. To be a viable beam steering technique, the array dynamics should naturally evolve toward the spatially uniform phase gradient state. By perturbing the desired solutions, $\phi_j = (j-1)\theta + \omega t + \eta_j$ where $\eta_j \ll 1$, a set of linear, ordinary differential equations (ODEs) describing the evolution of such perturbations can be constructed

$$\dot{\eta}_j = a\eta_{j+1} + b\eta_j + c\eta_{j-1} \quad (8)$$

where

$$a \equiv k\cos(\theta + \Phi) \quad (9a)$$
$$c \equiv k\cos(\theta - \Phi) \quad (9b)$$
$$b \equiv -(a + c) \quad (9c)$$
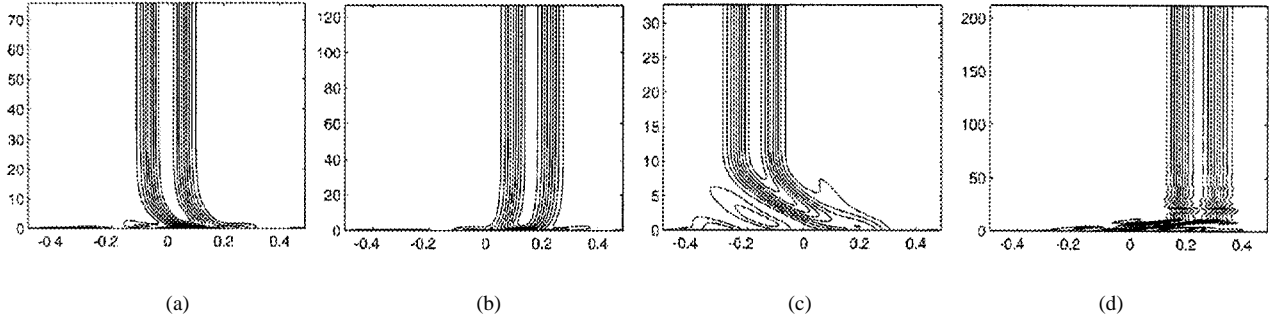
and

$$\eta_0 = \eta_{N+1} = 0. \quad (10)$$

Fig. 3. Time evolution (vertical) of a nonlinear active antenna array. These figures demonstrate beam steering for various coupling and phase gradient values for a seven-element, 1-D array. Plots (a) and (b) correspond to zero coupling phase ($\Phi = 0$), while plots (c) and (d) represent a nonzero coupling phase ($\Phi = \pi/4$). The phase gradients are (a) $\theta = 0$, (b) $\theta = \pi/3$, (c) $\theta = -\pi/3$, (d) $\theta = \pi/2$; the same set of random initial conditions was used in each. Stability analysis results are consistent with the observed transient effects.

A stable solution is one where the perturbations away from that state die out, i.e., $\eta_j \to 0$.[2] The eigenvalues of this set of linear ODEs describe how the various perturbation "modes" grow or decay; a stable solution is one where the real parts of the $N - 1$ nonzero eigenvalues are all negative. In the case of "static" beam steering, these eigenvalues can be computed analytically [22], [23]

$$\lambda_n = -2k' \left[1 - \cos\left(\frac{\pi n}{N}\right) \sqrt{1 - \tan^2\theta \tan^2\Phi} \right] \quad (11)$$

for $n = 1, \ldots, N - 1$ where $k' \equiv k \cos\theta \cos\Phi$. Analogous results can be written down in the case of time-dependent phase gradients, $\dot{\theta} \neq 0$ [22], [23]. Similar results have been obtained for an approximate, continuous array model as opposed to the inherently discrete element case being considered here [24], [25].

Establishing the existence and stability of the desired states of the system constitutes a complete solution to the beam steering problem. While these results were based on a simplified model, they provide significant insight into the capabilities of this novel beam steering technique. Some particularly interesting observations include the following.

1) The stability of a given beam steering state depends solely on the sign of k'. Consequently, a bifurcation does not arise from the operating frequencies or the number of elements N.
2) There is a limited range of realizable phase gradients. Assuming, for definiteness, that $\cos\Phi > 0$, the stable phase gradients are restricted to $\theta \in (\pi/2, -\pi/2)$. For half-wavelength spacing between array elements, this amounts to the ability to scan the main beam $30°$ off broadside. However, methods for extending this range to a full field of view have been proposed [26].
3) The eigenvalues (Lyapunov exponents) are proportional to the coupling strength. This means the greater the interaction between elements, the more rapidly the array will settle down to the desired state; conversely,

it will take longer to establish the uniform phase gradient across an array of weakly interacting elements.
4) As the number of elements increase, it takes longer for the array to reach the desired state, a consequence of the diffusive nature of the nearest-neighbor coupling.

Fig. 3 illustrates this beam steering method for the case of a seven-element array.

Although this analysis has focused on 1-D arrays, extension to rectangular ($N \times M$) 2-D arrays for steering in azimuth and elevation has been achieved [22], [23], [25]. In particular, it was found that steering is still accomplished by manipulation of the periphery elements alone, reducing the number of controls from NM to $2(N + M)$.

Also, the case of sinusoidal scanning has been addressed [22], [23]. For that case, a couple of interesting results emerged: 1) the technique was robust with respect to the scanning (sweep) frequency; in fact, the desired state was stable regardless of the scan rate and 2) a greater range of stable phase gradients occurs, increasing from $\pm 90°$ to $\pm 138°$.

B. Difference Pattern (Monopulse) Beam Steering

Difference patterns are key for tracking targets such as individual global positioning satellites or maintaining the placement of a null over a jammer. To produce a difference pattern, a slightly different phase distribution is required. In particular, for a 1-D array, there must be a π phase difference between the two halves. Thus, the desired solutions are now

$$\phi_j = (j - 1)\theta + \omega t + h_j \quad (12)$$

where

$$h_j \equiv \begin{cases} \pi & j > N/2 \\ 0 & j \leq N/2. \end{cases} \quad (13)$$

Obviously, the sum and difference pattern solutions are very simply related, i.e., $\phi_{diff} = \phi_{sum} + h_j$; yet, the beam steering scheme, as it stands, does not allow for the existence of the ϕ_{diff} solutions. Consequently, the array could not produce such an intensity pattern.

---

[2]As we are dealing with periodic orbits, there is a certain set of perturbations that leave one on the orbit, amounting to a time translation. Such perturbations do not render the state unstable.

However, it can be shown [27] that through a simple modification to the center-coupling link alone, a difference pattern may be established and controlled in the same manner as the sum pattern. To allow for such a modification, a variant of the phase model is introduced where the coupling phases can be manipulated

$$
\dot{\phi}_j = \omega_j + k\sin(\phi_{j+1} - \phi_j + \Phi_{j,\,j+1}) \\
+ k\sin(\phi_{j-1} - \phi_j + \Phi_{j,\,j-1}). \quad (14)
$$

Substitution of the desired difference pattern solution leads to

$$
\dot{\phi}_j = \omega_j + (-1)^{\delta_{j,\,N/2}} k\sin(\theta + \Phi_{j,\,j+1}) \\
- (-1)^{\delta_{j,\,(N/2)+1}} k\sin(\theta - \Phi_{j,\,j-1}) \quad (15)
$$

where $\delta_{i,\,j}$ denotes the standard Dirac delta function, i.e.,

$$
\delta_{i,\,j} \equiv \begin{Bmatrix} 1 & i = j \\ 0 & i \neq j \end{Bmatrix}. \quad (16)
$$

A careful inspection of these equations reveals a tremendous similarity to those encountered in the sum pattern problem. In fact, with the following choice of coupling phases

$$
\Phi_{i,\,j} = \begin{Bmatrix} \Phi + \pi & (i,\,j) = ((N/2)+1,\,N/2) \\ \Phi + \pi & (i,\,j) = (N/2,\,(N/2)+1) \\ \Phi & \text{otherwise} \end{Bmatrix} \quad (17)
$$

they become identical to those of the sum pattern analysis. Fig. 4 illustrates steering a monopulse beam.

In addition, incorporating these coupling phases into the linear stability analysis of the difference pattern solutions

$$
\dot{\eta}_j = a'\eta_{j+1} + b'\eta_j + c'\eta_{j-1} \quad (18)
$$

where

$$
a' \equiv (-1)^{\delta_{j,\,N/2}} k\cos(\theta + \Phi_{j,\,j+1}) \quad (19a)
$$
$$
c' \equiv (-1)^{\delta_{j,\,(N/2)+1}} k\cos(\theta - \Phi_{j,\,j-1}) \quad (19b)
$$
$$
b' \equiv -(a' + c') \quad (19c)
$$

again leads to identical stability matrices for the sum and difference pattern states.

Therefore, introducing a π phase shift in the coupling phase of the center link produces a difference pattern that can be steered in the same fashion as the sum pattern (i.e., by adjusting the natural frequencies of the periphery elements alone) and whose stability properties (settling time, bifurcation points, scan range) are identical to those of the sum pattern. As a result, it is possible to switch between the sum and difference patterns of the same coupled oscillator array. In passing, it is noted that rather than alter the coupling phase, reversing the sign of the coupling strength of the center-coupling link (i.e., $k \rightarrow -k$) could be used with identical results. Whether one chooses to adjust the coupling phase or coupling strength will depend on the feasibility of the particular approach.
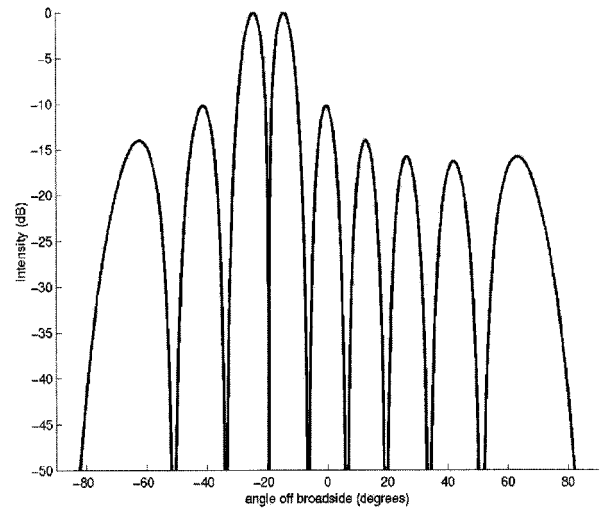

Fig. 4. Generating and steering a difference pattern for an 18-element, 1-D array. By a simple modification to a single coupling link, the beam steering technique developed for the sum pattern problem could also be used to steer a difference pattern. This figure was obtained via numerical integration of the dynamical equations with random initial conditions. The following parameters were used: $N = 18$, $\theta = \pi/3$, $k = 1$, and $\Phi = 0$.

C. Coupling Phase Beam Steering Method

An alternative method of beam steering can be formulated wherein the coupling phases rather than the oscillator natural frequencies are manipulated.

As phase-locked solutions are of interest, the synchronized oscillators will, by definition, possess a common frequency. Together with the condition of a spatially uniform phase gradient, the phase model (4) becomes

$$
\omega_1 = \omega + k\sin(\theta + \Phi_{1,\,2}) \quad (20a)
$$
$$
\omega_j = \omega + k\{\sin(\theta + \Phi_{j,\,j+1}) - \sin(\theta - \Phi_{j,\,j-1})\} \quad (20b)
$$
$$
\omega_N = \omega - k\sin(\theta - \Phi_{N,\,N-1}). \quad (20c)
$$

These relations specify the coupling phases

$$
\Phi_{i,\,j} = \begin{Bmatrix} -\theta & (i,\,j) = (1,\,2) \\ \theta & (i,\,j) = (N,\,N-1) \\ 0 & \text{otherwise} \end{Bmatrix}. \quad (21)
$$

Two points of interest arise from this result: 1) the coupling network between the end elements and interior elements must be nonreciprocal and 2) the simple linear relationship between the coupling phase and desired phase gradient. A similar approach has been previously documented, although that work did not address stability [28].

A linear stability analysis leads to the following set of coupled differential equations for the perturbations:

$$
\dot{\eta}_j = k(\cos\theta)^{(1-\delta_{1,\,j})(1-\delta_{N,\,j})}[\eta_{j+1} - 2\eta_j + \eta_{j-1}] \quad (22)
$$

where $\eta_0 = \eta_1$ and $\eta_{N+1} = \eta_N$. A closed-form analytic solution for the eigenvalues has yet to be obtained. However, apart from the overall coefficient of the η_1 and η_N equations,

the above set of linear differential equations is very similar to the following:

$$\dot{\eta}_j = k \cos\theta [\eta_{j+1} - 2\eta_j + \eta_{j-1}] \qquad (23)$$

whose eigenvalues are readily obtained

$$\lambda_n = -2k \cos\theta \left[1 - \cos\left(\frac{\pi n}{N}\right)\right] \qquad (24)$$

for $n = 0, \ldots, N - 1$. These eigenvalues provide a good estimate of the true values, especially as the number of elements becomes large.

Whether this manner of beam steering is preferred over that based on manipulating the oscillator natural frequencies depends on the application or implementation requirements; regardless, the possibility of two means to the same end provides the engineer with greater flexibility in the system's design.

D. Amplitude Dynamics and Sidelobe Reduction

As evidenced by their radiation patterns, phase model antennas generate relatively high sidelobe levels ($\sim$13 dB down from the main beam). This is to be expected since the assumption of identical amplitudes implies a uniformly illuminated array. However, for certain applications, such a sidelobe level is unacceptable and must be significantly reduced.

The conventional solution is to apply weighting (spatial tapering) of the element amplitudes. Several such weighting schemes exist, among those being cosine-on-a-pedestal, Dolph–Chebyshev, Taylor and Villeneuve. This section demonstrates how the oscillator amplitude dynamics can be controlled to achieve a desired amplitude profile across the array while the phase dynamics are used for beam steering. *Moreover, note that the simplifying assumptions leading to the phase model are not invoked here.* In particular, the amplitude and phase dynamics are allowed to evolve on similar time scales and the oscillator amplitudes now settle down to some nonuniform state specified by the weighting scheme used.

By relaxing the constraints on the amplitude dynamics, new opportunities are open to allow custom beam shaping, sidelobe suppression, and a possible trade between coupling and reduced array size [11]. Although extension to 2-D arrays is straightforward, simulation results are shown for 1-D oscillator arrays only.

To facilitate obtaining the requisite parameter values, the $2N$ real, ordinary differential equations (2) and (3) are expressed as a set of N complex ODEs by defining $z_j = A_j e^{i\phi_j}$

$$\dot{z}_j = (p_j + i\omega_j)z_j - |z_j|^2 z_j + ke^{i\Phi}[z_{j+1} + z_{j-1}]. \quad (25)$$

Solutions resulting in steered, low-sidelobe beam patterns are of the following form:

$$z_j = a_j e^{i(\omega t + [j-1]\theta)} \qquad (26)$$

where the a_j and θ are the desired amplitude weightings and phase gradient, respectively. Substitution into the above complex differential equations leads to a set of complex algebraic
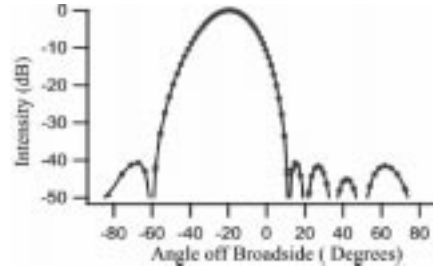

Fig. 5. Exploiting the amplitude dynamics of a seven-element array for sidelobe reduction. The solid lines denote the intensity pattern produced by Villeneuve amplitude tapering applied to a conventional, uncoupled array and the red circles represent the beam pattern of the coupled oscillator array. As this figure illustrates, the coupled oscillator array can be made to achieve the same performance as a conventional array design. The following parameters were used: $N = 7$, $\theta = 2\pi/5$, $k = 1$ and $\Phi = 0$. A Villeneuve weighting scheme was chosen to produce the -40-dB sidelobes; to this end, $\bar{n} = 4$ and a maximum value of $p = 10$ were utilized.

equations from which satisfying the real and imaginary parts defines how the p_j and ω_j should be adjusted

$$p_j = a_j^2 - \{K_{j,\,j+1}\cos(\theta + \Phi) + K_{j,\,j-1}\cos(\theta - \Phi)\} \quad (27)$$

$$\omega_j = \omega + (j-1)\dot{\theta} - K_{j,\,j+1}\sin(\theta + \Phi)$$
$$+ K_{j,\,j-1}\sin(\theta - \Phi) \qquad (28)$$

where $K_{j,\,j\pm1} \equiv k(a_{j\pm1}/a_j)$ and $a_0 = a_{N+1} = 0$. Note that, as expected, for the uniform amplitude distribution the natural frequency conditions reduce to those derived from the phase model. Fig. 5 illustrates a Villeneuve amplitude taper across a seven-element 1-D array of van der Pol oscillators. In Fig. 6, simultaneous beam steering and beam forming are demonstrated in a 17-element van der Pol array.

The linear stability analysis is most readily carried out through the original $2N$ real differential equations (2) and (3). Perturbing the desired solution $A_j = a_j + \xi_j$, $\phi_j = \omega t + (j-1)\theta + \eta_j$ where $\xi_j, \eta_j \ll 1$, one arrives at the problem of diagonalizing a stability matrix possessing a complicated structure.

Unlike the progress made in the phase model cases, this stability matrix's complexity and sensitive dependence on the weighting scheme chosen (including the desired sidelobe level), makes it seem unlikely that a closed-form analytic expression for the Lyapunov exponents could be obtained. However, numerical computation of the eigenvalues is straightforward. From such an approach, it seems that, in general, simultaneous beam shaping and beam steering results in a smaller range of stable phase gradient values. To what extent this reduction is attributable to the comparable time scales in the amplitude and phase dynamics as opposed to the nonuniformity in amplitudes is, at this time, an open question.

IV. Receiver Beam Forming Using Nonlinear Oscillators

In contrast to the previous section, this architecture is a hybrid approach that retains the traditional antenna beam forming elements, but inserts a coupled nonlinear oscillator
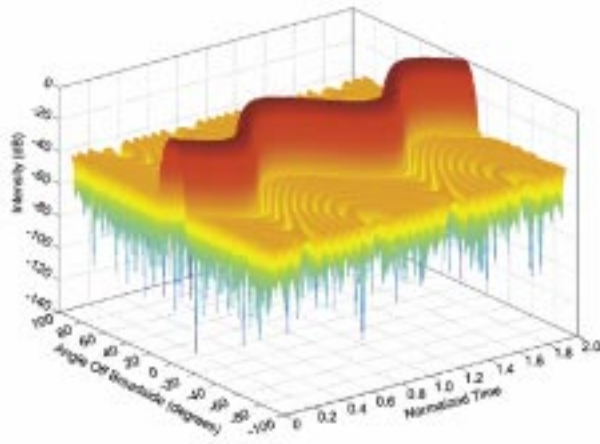
Fig. 6. Simultaneous sidelobe reduction and beam steering. Amplitude shaping does not come without cost. For the coupled nonlinear oscillators to encompass both the generation of low-sidelobe beam patterns and beam steering the parameter adjustments are more complicated; all elements must be manipulated. However, these parameter changes are via dc control line voltages to active antenna elements. This eliminates any RF control circuitry found in traditional phased array antennas. The following parameters were used: $N = 17$, $k = 1$, and $\Phi = 0$. Again, -40-dB sidelobes were produced via a Villeneuve weighting scheme where $\overline{n} = 9$ and the maximum $p = 10$. The main beam was sinusoidally scanned between $\pm \pi / 3$.
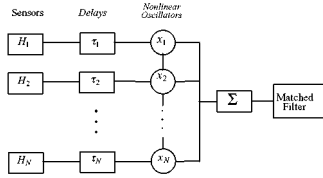

Fig. 7. Nonlinear narrow-band beam former. The hybrid architecture relies on the synchronization of the array of nonlinear oscillators to distinguish signals from clutter received from the linear front-end.

array to perform narrow-band beam forming for phased array receivers. A block diagram of this beam former is shown in Fig. 7.

The array of nonlinear oscillators is tuned so that the state in which the oscillators are phase-locked to the incident signal and each other exists only for plane waves incident within the main beam of the array. For waves outside the main beam, this synchronization does not occur and the individual oscillators are no longer phase-locked to the incident signal. Rather, they oscillate primarily at or near the average of their natural frequencies. These different dynamical regimes, not present in conventional linear beam forming, enable main beam and sidelobe signals to be distinguished on the basis of frequency.

A. Receiver Elements

The first elements in receiver block diagram are the sensors (H_i), e.g., hydrophones, antennas, etc., whose responses are assumed to be linear and have spacing d. Denoting the phase difference between adjacent sensor elements by $\Delta\varphi$, a

plane wave with wave number k incident at an angle θ relative to broadside will yield

$$\Delta\varphi = kd(\sin\theta - \sin\theta_0) \tag{29}$$

where θ_0 is the steering angle of the array. Beam steering is accomplished as in conventional beam formers either via the insertion of delays τ_i to the sensor outputs or by phase shifters. Separate beams will be formed in parallel requiring one channel per beam.

The (delayed) output of each sensor, H_i, is input as a driving force, $f_i(t)$, for its respective nonlinear oscillator whose state is denoted by $\mathbf{x}_i$. The components of the state vector $\mathbf{x}_i$ may be taken as the various voltages describing the circuit dynamics. The dynamics of each oscillator is governed by the system of nonlinear ordinary differential equations of the form

$$\dot{\mathbf{x}}_i = \mathbf{F}(\mathbf{x}_i, \mu_i) + \sum_j \boldsymbol{\kappa}_{ij}\mathbf{x}_j + f_i(t) \tag{30}$$

where $\mathbf{F}(\mathbf{x}_i, \mu_i)$ is a nonlinear function of $\mathbf{x}_i$. The parameters μ_i are chosen so that, when uncoupled, each oscillator $\mathbf{x}_i$ will undergo oscillations at its natural frequency ω_i. The second term on the right-hand side represents coupling between elements where κ_{ij} is the strength of the coupling from element i to element j. In the case of narrow-band signals, the forcing term, $f_i(t)$, can be considered to be a slowly modulated function around the carrier frequency, Ω, corresponding to the incident wave number k.

The outputs of the nonlinear oscillator array are summed and then input to a matched filter. The outputs are summed according to

$$s(t) = \sum_i w_i g(\mathbf{x}_i) \tag{31}$$

where $g(\mathbf{x}_i)$ is a linear function of one or more of the components of $\mathbf{x}_i$. The weights w_i can be used to taper the array if so desired. After forming a power spectrum, the matched filter then selects the frequency component of interest. Discriminating between signals incident on the main beam and sidelobes is discussed below. Note that if need be $s(t)$ can be demodulated prior to the downstream signal processing. It is also possible to have alternatives to a matched filter for the downstream signal processing.

B. Array Dynamics

For simplicity, assume that the array is steered to broadside ($\theta_0 = 0$) in the following description of the array dynamics. A monochromatic plane wave of frequency Ω, wave number k, and amplitude a_0 is taken to be incident upon the array at direction θ. The parameters μ_i or the coupling strengths $\boldsymbol{\kappa}_{ij}$ can be set so that when the phase lag between oscillators is less than a certain critical phase lag, $|\Delta\varphi| < \Delta\varphi_c$, the array synchronizes and oscillates at the incident frequency Ω. By (29), this phase lag condition is equivalent to a limitation on the angle of incidence, $|\theta| < \theta_c$. When the phase lag exceeds $\Delta\varphi_c$, there is no synchronization with the incoming

signal. Instead, the individual oscillators oscillate at or near the average or compromise frequency, $\overline{\omega}$, of their natural frequencies and the phase relationships between them are not constant. A signal incident within the main beam, $|\theta| < \theta_c$, has a power spectrum centered around the plane wave frequency of interest, whereas a signal incident in the sidelobes, $|\theta| > \theta_c$, has a spectrum distributed primarily around $\overline{\omega}$ with side peaks corresponding to the nonlinear mixing between the incident and natural frequencies. Thus, a frequency-domain matched filter can readily determine whether a signal is incident in the main beam or the sidelobes. This is not the case for linear beam forming where both main beam and sidelobe signals cause the array to respond at the signal frequency Ω, and so frequency cannot be used to discriminate them. In order for the dynamics to play out as just described the natural frequencies ω_i must not be too disparate from each other or the signal frequency Ω.

A numerical simulation of the response of the nonlinear oscillator array to an incident narrow-band signal, and a system of N nonlinear oscillators with nearest-neighbor coupling was simulated. The dynamics obeyed by each oscillator were chosen to be that of a forced, weakly nonlinear van der Pol oscillator [29]–[33]

$$\dot{z}_i = (\alpha + j\omega_i)z_i - |z_i|^2 z_i + \kappa(z_{i+1} + z_{i-1} - 2z_i)$$
$$+ a(t)e^{j(\Omega t + \varphi_i)}, \qquad i = 2, \dots, N-1 \quad (32)$$

where z_i is a complex quantity describing the state of the ith oscillator, α is the excitation coefficient, κ is the coupling coefficient, Ω, and φ_i are the input signal frequency and phase, and $a(t)$ is a complex amplitude factor which can allow for slow changes (relative to the oscillation period) in the magnitude or phase of the incoming signal. Free-end boundary conditions are used so that the first and last elements obey (33a) and (33b), respectively. Note that these equations are in dimensionless form

$$\dot{z}_1 = (\alpha + j\omega_1)z_1 - |z_1|^2 z_1 + \kappa(z_2 - z_1)$$
$$+ a(t)e^{j(\Omega t + \varphi_1)}, \qquad i = 1, \quad (33a)$$
$$\dot{z}_N = (\alpha + j\omega_N)z_N - |z_N|^2 z_N + \kappa(z_{N-1} - z_N)$$
$$+ a(t)e^{j(\Omega t + \varphi_N)}, \qquad i = N. \quad (33b)$$

For the following results, the delays have been set to zero so that the array is steered to broadside. Fig. 8 shows the simulation results for a beam former with eight elements in response to an incoming monochromatic plane wave, $f_i(t) = a_0 \exp\{j(\Omega t + (i-1)\Delta\varphi)\}$, incident just off the beam axis. The frequency of the input signal is $\Omega = 1.2$ and the oscillator natural frequencies were all taken to be identical so that $\omega_i = \omega = 1.0$. The phase difference between adjacent elements is $\Delta\varphi = 0.2$ radians, which corresponds to an angle of incidence of $\theta = 3.7°$ for half-wavelength spacing. The input signals (the real part) to each of the eight oscillators are shown in the top panel and the phase difference between inputs can be seen in the offset of the curves. The output of each of the oscillators (taking the real part of z_i) is shown in the middle panel. The oscillators start out with random initial conditions but they quickly synchronize and maintain this synchronization, as can be seen by the constant phase
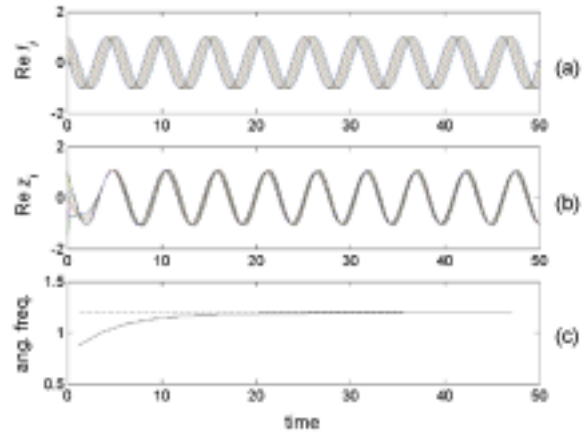

Fig. 8. Response of oscillator array to a main beam signal. (a) Inputs to oscillators. (b) Oscillator outputs. (c) Input frequency (dashed) and output frequency (solid). The signal parameters are $\Omega = 1.2$, $a_0 = 0.25$, $\Delta\varphi = 0.2$. The oscillator parameters are $\alpha = 1.0$, $\omega = 1.0$, $\kappa = 2.0$.
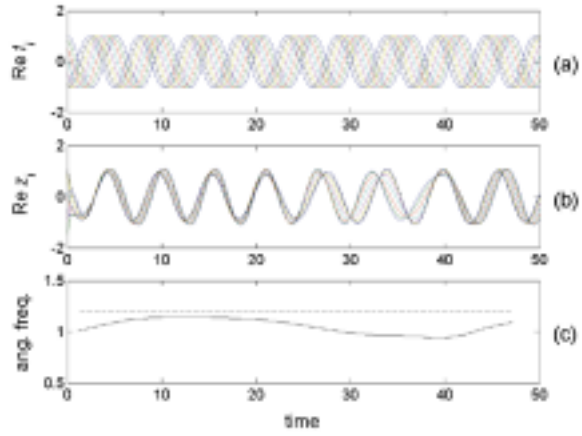

Fig. 9. Response of oscillator array to a sidelobe signal. (a) Inputs to oscillators. (b) Oscillator outputs. (c) Input frequency (dashed) and output frequency (solid). The parameters are the same as in the previous figure except $\Delta\varphi = 0.5$.

difference between curves. Note that this phase difference is less than for the input signals, which enables the main beam of the nonlinear beam former to have a flatter response than the equivalent linear beam former (see Fig. 10). The bottom panel shows the frequency of the input and output as a function of time where the array output is given by

$$s(t) = \text{Re}\left\{\sum_i z_i(t)\right\}. \quad (34)$$

After a brief transient, the output frequency rises to the input frequency. Since the output remains synchronized, this signal would be classified as being in the main beam of the nonlinear oscillator beam former. A remark concerning the signal amplitude is in order here: the amplitude $a_0 = 0.25$ was chosen to be above the threshold for oscillations required for synchronization. This threshold is given by $|\Omega - \omega| = 0.2$ as can be shown from consideration of the phase equations corresponding to (32) and (33).
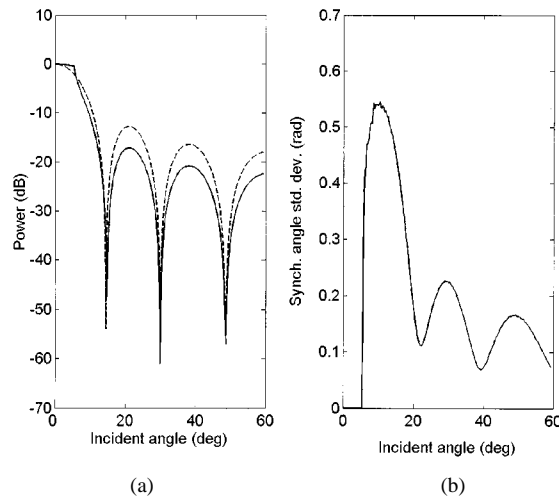
Fig. 10. (a) Response of nonlinear beam former as a function of angle of incidence for an array steered to broadside (solid) compared with response of linear beam former (dashed). (b) Standard deviation of synchronization angle. Parameters are the same as for the previous figures except $\Delta\varphi$ was varied between 0 and 2.7.

Fig. 9 shows the beam former dynamics in response to a signal that lies in the sidelobe of the nonlinear oscillator beam former. The phase difference between the inputs to adjacent oscillators is $\Delta\varphi = 0.5$ corresponding to an angle of incidence of $\theta = 9.2°$ assuming half-wavelength spacing. All other parameters are the same as in Fig. 8. The input signals shown in the top panel have a wider spacing between them than in Fig. 8 due to the larger phase difference. The middle panel shows the eight oscillator outputs, which, as can clearly be seen, do not remain synchronized, i.e., the phase difference between outputs changes with time. In the bottom panel, the frequency of the output does not match the input signal frequency, rather, it oscillates around the natural frequency with a frequency of $\Omega - \omega = 0.2$. Accordingly, this signal would be classified as being outside the main beam of the nonlinear oscillator beam former. However, the angle of incidence of $\theta = 9.2°$ is within the main beam of the equivalent untapered eight-element linear beam former whose first null is located at $14.5°$. This indicates the improved resolution possible with the nonlinear oscillator beam former.

Fig. 10(a) shows the response of the nonlinear oscillator beam former to a fixed amplitude plane wave signal as the angle of incidence is varied (assuming half-wavelength spacing between elements). The array is steered to broadside. The response is found from the output power spectrum at a given angle of incidence by calculating the power contained in a small interval around the input frequency Ω and then normalizing so that the response at $\theta = 0°$ is equal to one (0 dB on the plot). Also shown is the beam pattern that would be produced by the equivalent untapered conventional linear beam former. It can be seen that the nonlinear oscillator beam former possesses a narrower and flatter main beam and lower sidelobe levels than does the conventional beam former. Note, however, that the response of the nonlinear oscillator beam former to a given signal will depend nonlinearly on its amplitude and the presence

of other signals. The sharp corner on the main beam of the nonlinear oscillator beam pattern can identify the critical angle of incidence, above which the coupled oscillator array will not synchronize. It is approximately 5°, which corresponds to a critical phase difference of $\Delta\varphi_c = 0.27$ radians. This can be seen more directly in Fig. 10(b), where the standard deviation of the synchronization angle χ is plotted. χ is defined by

$$\chi = \arg\left(\sum_i e^{j(\psi_i - \psi_1)}\right) \quad (35)$$

where $\psi_i = \arg(z_i)$. If the oscillators always have constant phase differences with each other, then χ will be constant and its standard deviation will be zero. If the oscillators are not phase-locked, χ will vary over time and its standard deviation will be nonzero. So Fig. 10(b) clearly shows the abrupt loss of synchronization at about 5°.

Results obtained are similar to those above for amplitude modulated and linear frequency modulated signals provided that the threshold condition is not violated. There remains much to be investigated before the utility of this beam-forming concept can be assessed, particularly with regards to its performance in the presence of noise and interference.

V. Exploiting Microelectronics in the Study of Nonlinear Active Antennas

A. Modeling Nonlinear Antenna Dynamics Using aVLSI

A common thread throughout this research is the application of recently developed analytical and experimental tools toward the study and control of nonlinear systems. Analog microelectronics is an effective tool for examining both the physics and engineering questions that arise in coupled nonlinear arrays. Analog very large scale integration (aVLSI) provides the dynamicist with a flexible and low-cost technology for the construction of large-scale nonlinear arrays. The ability to place thousands of individual elements, capable of computing a complicated function or representing a dynamical nonlinear system, in a single low-cost and compact device is a powerful experimental tool [34].

Even though aVLSI designs often incorporate digital components, it is the abandonment of the many layers of abstraction involved in digital design that empowers the aVLSI engineer. The design philosophy begins by using the transistor not as a simple switch but as an analog device capable of performing computation. This allows aVLSI designers to increase the level of integration by employing simple, nonlinear computation elements working collectively to perform a specific task. This design strategy is widely used in focal plane arrays (optical sensors) for enhancing pattern recognition [35]. One of the research goals is to mimic these designs at microwave frequencies to form a signal processing layer at the plane of radiation collection (or transmission) to improve antenna beam pattern recognition. However, the design, fabrication, and testing of microwave active antennas requires a substantial investment of time
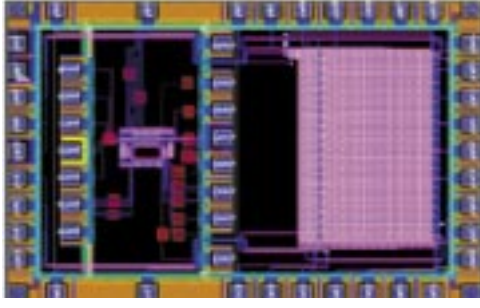
Fig. 11. CMOS nonlinear array designed and fabricated in a 0.35-μm process (TSMC). The chip layout shows several 1-D arrays (stacked) on the bottom portion of the chip.

Fig. 12. Block diagram of the nonlinear oscillator design. The design is a modified second-order filter and is constructed from amplifiers that have adjustable linear regions as well as operational current levels. The circuit operates as a nonlinear oscillator by employing the inherent nonlinear qualities of the feedback amplifier q. The amplifiers τ_1 and τ_2 typically operate in the linear regime.

and money. Fabrication of a monolithic antenna operating in the gigahertz range can cost $50 000 or more. With many physics and design questions yet to be answered, scaling the nonlinear design down to audio frequencies allows the use of affordable aVLSI foundry services. As a result, the experiments reported here use low-frequency (kHz) aVLSI to test prototype nonlinear array designs.

Arrays of nonlinear oscillators have been designed and fabricated using a number of different CMOS processes. Scalable design rules are used to minimize the difficulties involved with moving the design between different processes. However, all the results presented in this section are obtained from a 0.35-μm CMOS design fabricated using the TSMC process. Fig. 11 shows the general layout of the design. The chip contains several rows of 20 elements each stacked on top of each other (right half of layout). Each row consists of a 1-D array of coupled nonlinear oscillators employing local linear coupling. The entire array is partitioned for different sizes of arrays varying from 20 to 80 elements.

Sections V-B and V-C discuss the unit cell for the nonlinear array. The unit cell is based on a modified second-order section with an the adjustable wide linear range amplifier (WLA) as its fundamental building block [36]. An analytical model of the unit cell is developed and then related to the to the van der Pol system. Sections V-E and V-F review the experimental methodology and compare measured results to simulation predictions. The goal of the experimental aVLSI work is to characterize unit cell parameters to match the equations of motion for the weakly nonlinear van der Pol oscillator and to demonstrate a proof of concept for nonlinear beam forming and beam steering techniques.

B. van der Pol Oscillator as Array Unit Cell

The van der Pol oscillator, represented by (36), is an excellent choice for the unit cell because it exhibits many of the behaviors that are required for nonlinear beam steering and beam forming, including the weakly nonlinear phase and amplitude dynamics described in (2) and (3). The van der Pol equations in standard form is clearly two dimensional, meaning that its state in time is fully described by two variables. In order to construct a unit cell from transconductance amplifiers requires reducing the second-order ODE into two
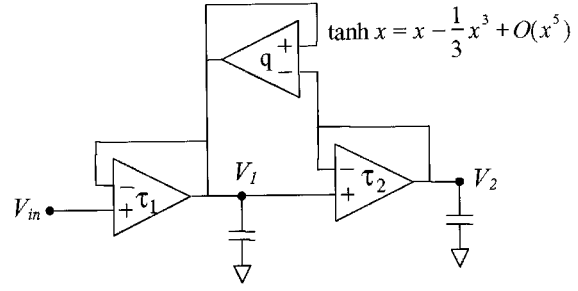
equivalent single-order ODEs, (37) and (38). Voltages now represent the state variables

$$\ddot{x} = \mu(1 - \eta x^2)\dot{x} - x \tag{36}$$
$$\dot{x} = w + \mu F(x) \tag{37}$$
$$\dot{w} = -x \tag{38}$$
$$F(x) = x - \eta \tfrac{1}{3} x^3. \tag{39}$$

The unit cell is based on a second-order filter (second-order section [34]) show schematically in Fig. 12. The unit cell differs from a more traditional filter by employing the nonlinear qualities of the transconductance amplifier. Typically this is accomplished by making the linear range of the feedback amplifier (labeled q in Fig. 12) narrow relative to the feedforward amplifiers (V_- and V_+). To accommodate the need for this adjustable nonlinearity, the WLA allows the width of the linear transconductance region and bias current to be varied. The design is based on an above-threshold differential pair, whose currents are renormalized by diodes and a below-threshold differential pair.

For the WLA, the linear range and bias current of each amplifier is an accessible parameter set by V_l and V_b. In particular, the V_b parameter sets a bias current (overall operating current) that follows a similar transfer curve to a subthreshold CMOS transistor. As a result, there is an exponential relationship between the input voltage V_b and the output current I_{out}. This allows the oscillator to function at low current levels while at the same time running at frequencies that span many orders of magnitude.

Equation (40) models the WLA

$$I_{out}(V_+, V_-) = B(V_b)\tanh(A(V_l)(V_+ - V_-)) \tag{40a}$$
$$A(V_l) = \frac{\alpha}{V_l - V_t} \tag{40b}$$
$$B(V_b) = I_0 e^{\beta V_b}. \tag{40c}$$

The parameters α, V_t, β, and I_0 are dependent on the fabrication process and are fixed. The process-dependent parameters were measured from a test amplifier fabricated on the 0.35-μm chip: $\alpha = 1.3$, $V_t = 0.62$ V, $\beta = 20.34$ V^{-1}, and $I_0 = 1.47 \ 10^{-15}$ A. The parameter α is a dimensionless quantity.

Fig. 13 shows example measurements from a test amplifier for two different values of V_b and V_l (solid lines). These measurements were made using a source-measure unit (Keithley 236) (SMU) capable of sourcing a voltage and accurately measuring current at a node. The output of the amplifier was connected to the inverting input V_- and held at a fixed voltage of 1.7 V. The output current was measured as a function of the input voltage V_+ (see inset of Fig. 13). The dashed lines show the predicted response using (40a) and the measured system dependent parameters. Equation (40) for the WLA does not capture all the experimental features, most notably the undesirable voltage and current offsets.

C. Unit Cell Description

Using Kirchhoff's law and Fig. 12 as a guide, a set of equations (41) and (42) describing the unit cell are derived. The output current from the respective amplifiers in Fig. 12 are $I_{\tau 1}$, $I_{\tau 2}$, and I_q. The system equations of motion are given by

$$C\dot{V}_1 = I_{\tau 1}(V_{in}, V_1) + I_q(V_1, V_2) \tag{41}$$
$$C\dot{V}_2 = I_{\tau 2}(V_1, V_2). \tag{42}$$

To simplify the analysis, the equations of motion are recast into dimensionless form by a change of variables. Substituting $V_a = V_2 - V_1$ into (41) and (42) yields (43) and (44)

$$\frac{C}{A_\tau B_\tau} \dot{V}_a = -2V_a - V_{in} + \frac{I_q(V_2 - V_a, V_2)}{A_\tau B_\tau} \tag{43}$$
$$\frac{C}{A_\tau B_\tau} \dot{V}_2 = -V_a. \tag{44}$$

Assuming τ_1 and τ_2 are linear amplifiers and q functions in a weakly nonlinear region, the feedback current V_a can be expanded to third order. Finally, scaling time by the factor $C/A_\tau B_\tau$ and writing the parameters μ and η in terms of the experimental parameters A_τ, B_τ, A_q, and B_q, (45) and (46), yields the familiar van der Pol oscillator (36)

$$\mu = \frac{A_q B_q}{A_\tau B_\tau} - 2 \tag{45}$$
$$\eta = \frac{A_q^3 B_q}{A_q B_q - 2A_\tau B_\tau}. \tag{46}$$

In the unit cell model, the fabrication-dependent parameters for τ_1 and τ_2 are assumed identical, allowing the oscillator operating frequency to be set directly by the scaling time. In the van der Pol equation, μ controls the strength of the nonlinear term, determines the stability of the oscillator, and defines the region where the phase model is valid ($0 < \mu < 1$). The system amplitude dynamics is controlled by η. There is now a one-to-one correspondence between the unit cell equations of motion and the van der Pol equation. Although μ and η allow direct comparison to the van der Pol oscillator, they are functions of all the transconductance amplifier parameters A_τ, B_τ, A_q, and B_q. Ultimately, control over the amplifier's accessible parameters is set by $V_{l\tau}$, $V_{b\tau}$, V_{lq}, and V_{bq}.
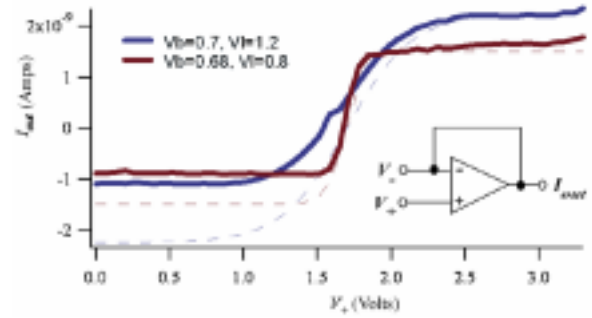

Fig. 13. Wide linear range amplifier measurements compared to model predictions. The design of the WLA allows experimental control over the linear transconductance region as well as the overall bias current level. The figure shows experimental measurements (solid lines) from a test amplifier on the 0.35-μm chip for two different values of V_i and V_b, which set the width of the linear region and the saturation levels, respectively. The dotted lines show the predicted curves from the amplifier model.

D. Modeling the Nonlinear Array

Given the measurable process dependent parameters α, V_t, β, and I_0, the system can be modeled using the reduced analytical form of (43) and (44). By directly integrating (45), the feasibility of using the experimental system as a nonlinear oscillator array capable of demonstrating steering can be explored. Plots from numerical simulations are shown in Fig. 14. In the simulations, the frequency of the boundary elements are detuned by adjusting their bias currents via the parameter $V_{b\tau}$. The figure shows that the ideal system is capable of demonstrating the beam steering effect.

In the experimental system, local linear coupling is achieved by using two additional amplifiers in the design of the nonlinear oscillator. Each oscillator has an additional amplifier for measuring the difference between its left and right nearest-neighbor voltages, in this case V_1, and to provide a proportional current feedback. In terms of the model equations, the 1-D array can be represented by (47) and (48). For local linear coupling, the size of the linear region of the coupling amplifiers is assumed to be large compared to the feedback amplifier

$$C\dot{V}_i = I_{\tau_i}(V_{in}, V_{1_i}) + I_{q_i}(V_{1_i}, V_{2_i})$$
$$\qquad + I_{cl}(V_{1_{i-1}}, V_{1_i}) + I_{cr}(V_{1_{i+1}}, V_{1_i}) \tag{47}$$
$$C\dot{V}_{2_i} = I_{\tau_i}(V_{1_i}, V_{2_i}). \tag{48}$$

A 20-element chain is numerically simulated using the above equations along with measured process-dependent parameters. Fig. 14 illustrates a time series. In the figure, the intensity level represents the value of V_1 for each oscillator as a function of time. At $t = 0$, the oscillators have a random distribution of initial conditions. They quickly synchronize to an oscillating pattern with equal phase distribution between oscillators. At $t = 2.4$ s, the parameter $V_{b\tau}$ for each oscillator is set across a gradient. At $t = 4.8$ s, the gradient is reversed. The array quickly settles to a new nonuniform phase distribution. The curvature in phase distribution is due to the fact that the bias current of the WLA is exponentially dependent on the parameter V_b, reflected in an exponential change
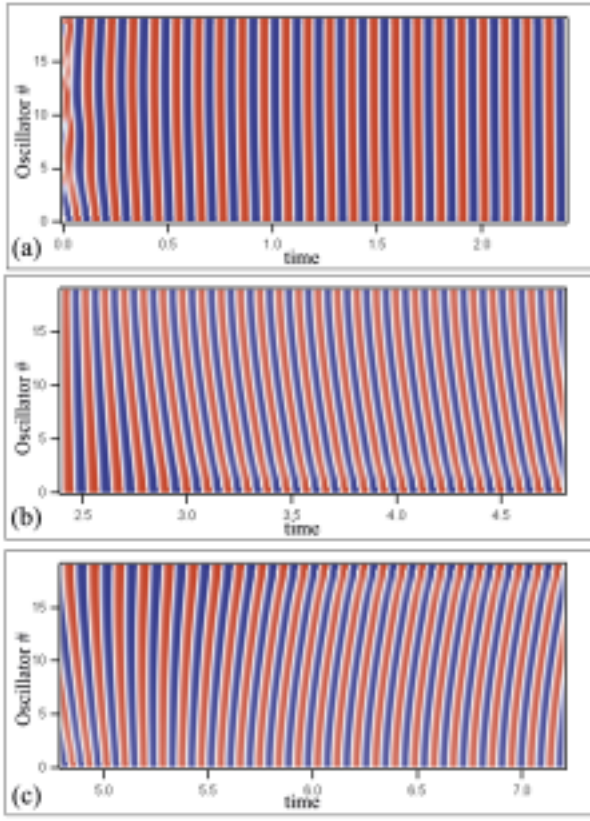
Fig. 14. Numerical simulation of coupled 20-element array. The frequencies of the boundary elements are detuned to generate the phase gradient. The intensity level represents the value V_{1_i} for each oscillator as a function of time. At $t = 0$, the oscillators have a random distribution of initial conditions. They quickly synchronize to an oscillating pattern with zero phase difference between oscillators. At $t = 2.4$ s, the parameter $V_{b\tau}$ for each oscillator is set across a gradient so that $V_{b\tau_0} = 0.705$ and $V_{b\tau_{19}} = 0.695$. The other system parameters are $V_{l\tau} = 1.2, V_{lq} = 0.72, V_{bq} = 0.68$, $V_{lc} = 1.2, V_{bc} = 0.68$. At $t = 4.8$ s the gradient is reversed. The array is quick to settle to new phase distributions.

in natural frequency. This mimics the design of the experimental array. Despite the drawbacks of this design feature, the numerical model captures the qualitative features of frequency and phase synchronization. In the figure, $V_{l\tau} = 1.2$, $V_{b\tau} = \{0.7, 0.695, 0.705\}$, $V_{lq} = 0.72$, $V_{bq} = 0.68$.

E. Experimental Design and Interface

Initial results are limited to tests from chips containing 20-element arrays, a test amplifier, and a single unit cell. The test amplifier and unit cell were used to characterize the fabrication process.

One of the problems of analog IC design is obtaining access to a large number of state variables given a limited number of pins. A common solution for this problem is to time-multiplex the desired signals to a small number of pins. In measuring the state of a large array of coupled oscillators such multiplexing is further complicated by the need to measure relatively small phase differences between the each oscillator, which requires fast access to each node in the array.
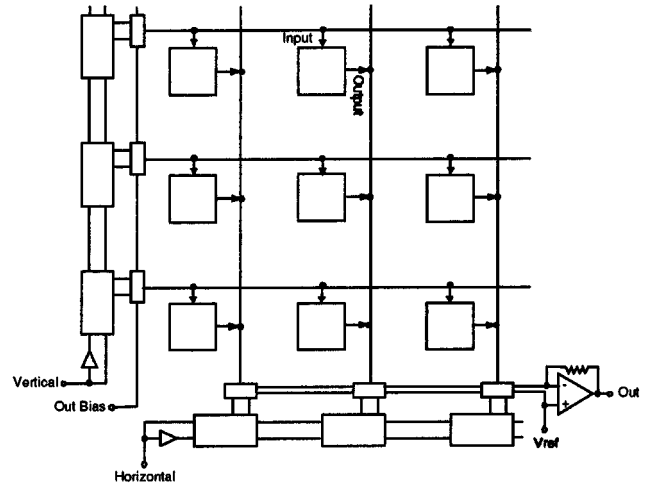

Fig. 15. Scanning circuitry block diagram. In the style of Mead *et al.*, we use a row column selection scheme that incorporates horizontal and vertical shift registers and differential current mode output was used. An external operational amplifier is used to convert the scanned current into a measurable voltage.

A simple scheme for time-multiplexing is to sequentially scan every element in the array, that is, to do a linear scan of the whole array, row by row. This is implemented by shift registers on the periphery of the array and pass devices for each measured variable, both in each element and on each row. Given the required scanning speeds, a differential current scanning method [37] is used, where currents are switched between lines at identical voltages, thus eliminating the capacitive loading effects.

The problem remains of translating the state variables, node voltages, into a current representation suitable for output. With the addition of one transistor, the output current from the WLA can be duplicated. The resulting measurement is the differential input voltage to the amplifier multiplied by a gain factor. The source voltage of the current mirror determines the gain. For these experiments the output of the feedback amplifiers are mirrored, making $G(V_{in} - V_1)$ and $G(V_1 - V_2)$ the measured quantities (see Figs. 12 and 15).

For additional flexibility on layout reuse, and at a minimum increase in layout size, the differential scan currents are multiplexed yet again at the edge of the array, leaving the final connection to the dummy voltage line at a single point just before leaving the chip. A single external data line and two clock lines directly drive the shift-registers. This allows row first or column first scanning or simultaneous readout using an external operational amplifier to convert the current into a measurable voltage. This scheme is illustrated in Fig. 15.

A certain amount of flexibility is desired from the electronic interface to the chip. Ideally all system parameters are accessible and all state variables can be measured instantaneously without complicating the process of experimentation. For simplicity, all the complications of operating the scanning circuitry have been abstracted with a group of simple commands that are interpreted by a microcontroller.
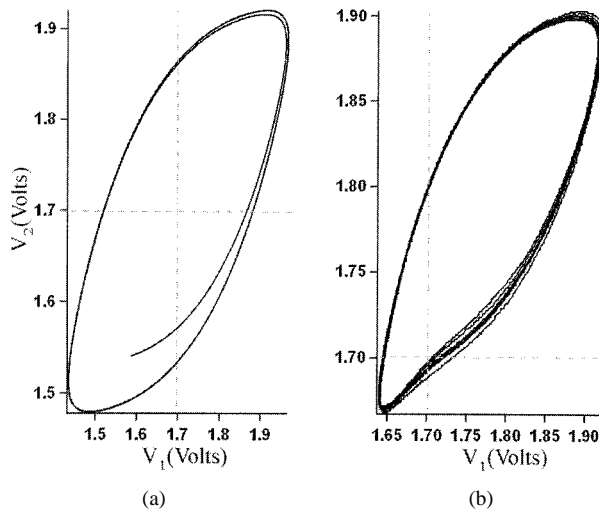
Fig. 16. Numerical and experimental phase space measurements. (b) Example experimental phase space diagram compared with (a) one generated using the model system. Significant amplifier offset, which is evident in the experimental plot, is the result of parameter mismatch between transistors in the design. In both plots $V_{l\tau} = 1.2, V_{b\tau} = 0.7, V_{lq} = 0.72$, and $V_{bq} = 0.68$.

Separate interface cards were used for analog-to-digital conversion (ADC) and digital-to-analog conversion (DAC).

A microcontroller was used to interpret commands from the personal computer (PC), control the scanner clock and data lines for row–column selection, and signal the PC when the scanned output current is ready for measurement. On the PC side, communication with the microcontroller (Microchip PIC16C84) is handled via input/output (I/O) ports on the DAC card (National Instruments 6052E). Commands are received as interrupts on a digital I/O port. The commands are then interpreted as modes. For example, in one mode the microcontroller scans the state of the entire array. Alternatively, there is a mode for scanning individual rows in the array and a mode for selecting individual elements. When state variables are being scanned from the array, the data acquisition card receives a trigger signal from the microcontroller each time a new value is available for measurement.

F. Experimental Measurements

Phase space measurements were made on a unit cell that enables direct comparison between the experimental measurements and the numerical predictions of the model, alleviating the need to convert the scanned currents into the state variables V_1 and V_2. Fig. 16 depicts an example experimental phase space diagram (right), compared with one generated using the model system (left). The two plots compare well quantitatively. A significant and undesirable quality of the physical system is amplifier offset due to parameter mismatch between transistors in the design. This is evident in the offset in the experimental plot. In both plots $V_{l\tau} = 1.2$, $V_{b\tau} = 0.7$, $V_{lq} = 0.72$, and $V_{bq} = 0.68$.

Examining the Jacobian of the model can make predictions of the nonlinear oscillator's behavior. The Jacobian for the reduced nonlinear oscillator, represented by (37)–(39), is shown in (49)

$$\mathbf{A} = \begin{pmatrix} \varepsilon - \eta x^2 & 1 \\ -1 & 0 \end{pmatrix}. \tag{49}$$

The eigenvalues of the Jacobian evaluated at the origin determine the stability of the fixed point. The trace τ and determinant Δ are given by (50)

$$\lambda_{1,2} = \tau \pm \sqrt{\tau^2 - 4\Delta}. \tag{50}$$

For the reduced model, which is an amplitude and time-scaled van der Pol oscillator, the trace is $\tau = \mu$, and is given in terms of the experimental parameters by (45). For this system the determinant is 1, so the fixed point dynamics are limited to stable and unstable spirals and nodes and unstable spirals and nodes [38]. The fixed point behavior of the numerical model is mapped by the stability diagram shown in Fig. 17(a). In the figure the linear amplifier parameters are $V_{l\tau} = 1.2$, $V_{b\tau} = 0.7$. Stability is determined by the parameters V_{lq} and V_{bq} of the feedback amplifier. Regions of different colors represent different dynamic behavior. Red indicates stable fixed point behavior, where $\tau < 0$. White indicates unstable spirals, where $0 < \tau < 2$. Blue indicates an unstable node, where $\tau > 2$. In the diagram the onset of oscillation is at the border between the red and white regions. The weak nonlinear behavior of the reduced system, which can be approximated by a phase and amplitude model, is defined by the region of parameter space where $0 < \tau < 1$.

Similar plots for the experimental system are shown in Fig. 17(b) and (c). The experimental parameters $V_{l\tau}$ and $V_{b\tau}$ are the same as in Fig. 17(a). The experimental state space diagrams are also defined by the same range of values for V_{lq} and V_{bq}. The diagrams are made by plotting the standard deviation of a time series measurement of $I_{\tau 1}$ for each value of V_{lq} and V_{bq}, keeping in mind the amplitude of oscillation in the reduced system is also determined by the spatial scaling parameter η, which is a function of all the system parameters.

Qualitatively the diagrams agree with the theoretical predictions in that the boundary separating the regions of stable fixed point behavior and oscillation is similar in all the diagrams. The most significant difference between the two experimental diagrams is the specific location of the boundary region. Because the weakly nonlinear region of parameter space is relatively narrow, any variation between elements in the array results in operation outside this region. The theory is predicated on the weakly nonlinear description of the van der Pol oscillator and the current unit cell design while providing proof of concept, is not ideal.

Despite the parameter variation in the unit cell design, the 20-element 1-D arrays chip were able to demonstrate frequency and phase synchronization and beam steering with strong nearest-neighbor coupling (Fig. 18). Unfortunately, variation in the fabrication process had a negative effect on the operation of the array. For example slight variation in the system parameters, such as the parameters α, V_t, β and I_0 used in the numerical model, can cause a wide variety of behavior for a common global system parameter, such as V_b and
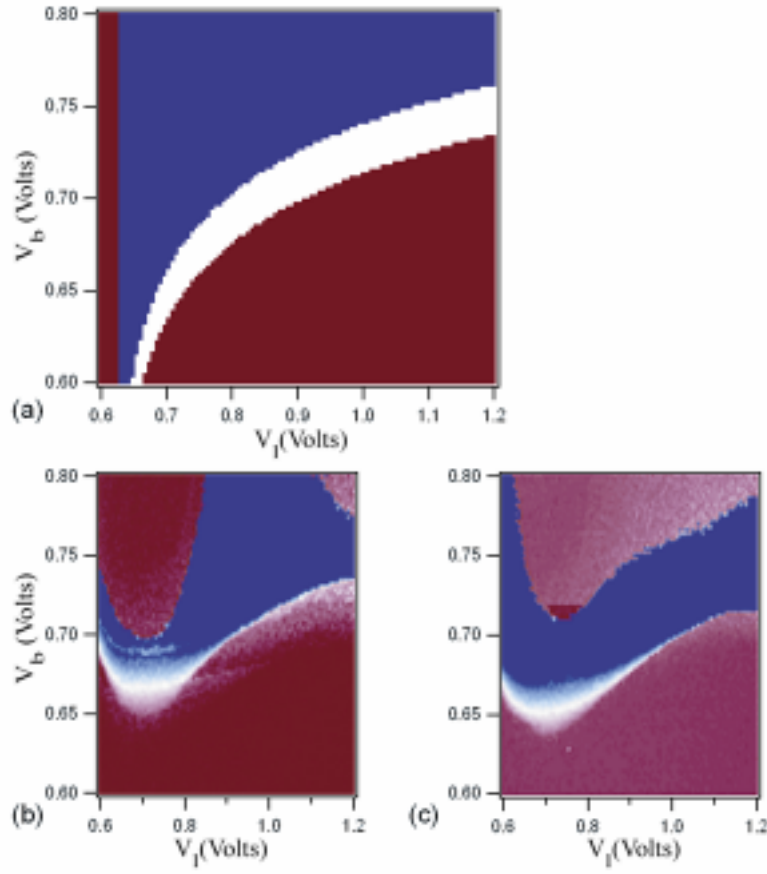
Fig. 17. (a) Analytical stability diagram and (b) and (c) experimental state space diagrams. The stability diagram represents a variety of fixed point behaviors for the reduced system. Red indicates a stable fixed point ($\tau < 0$). White indicates unstable spirals ($0 < \tau < 2$). Blue indicates an unstable node ($\tau > 2$). The experimental state space diagrams (b) and (c) are measured from array elements at row 4, column 7 and row 9, column 6, respectively. The diagram is made by measuring the standard deviation of the measured current $I_{\tau 1}$ plotted as a function of V_{l_q} and V_{bq}. The most significant difference between the two experimental diagrams is the specific location of the boundary region. Mismatch between oscillators (i.e., offsets) results in a number of elements exhibiting strong vice weak nonlinear behavior.
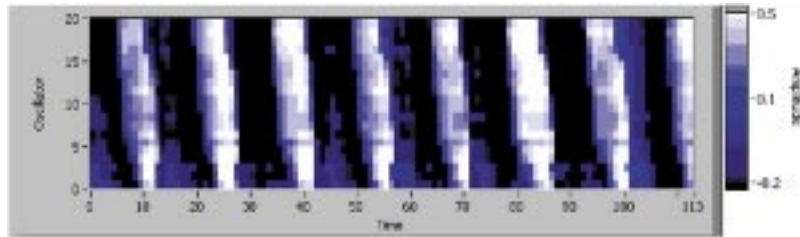

Fig. 18. Experimental beam pointing in a 1×20 analog VLSI array. Frequency and phase synchronization using strong nearest-neighbor coupling. The natural running frequency of each element is set along a gradient, so the top element in the array has a natural frequency that is less than the natural frequency of the bottom element. With strong coupling, all the elements synchronize to a common frequency with a constant phase difference between oscillators.

V_l. This effect is dominated by the system's exponential dependence on the process dependent parameter I_0 as evident in the phase space diagrams in Fig. 16 and the state space diagrams in Fig. 17(b) and (c).

In order to perform coherent phase and frequency synchronization, it was necessary to employ strong coupling between oscillators. Nevertheless, beam pointing in a coupled array of nonlinear oscillators was clearly demonstrated. The natural frequencies were tuned with the parameter $V_{b\tau}$, along a gradient, so the top element in the array has a natural frequency that is less than the natural frequency of the bottom element. With strong coupling, all the elements synchronize to a common frequency with a constant phase difference between oscillators.

VI. SUMMARY

It was demonstrated how to exploit the interactions between coupled, nonlinear elements to produce a desired far-field radiation pattern. In particular, sum and difference beam pattern steering along with amplitude tapering for sidelobe reduction were addressed. To this end, the response of a coupled, nonlinear oscillator array to adjusting various system parameters was explored. A nonlinear beam steering array was realized using analog microelectronics.

This novel approach indicates the ability to utilize the inherent, interactive dynamics of the phased array to achieve performance similar to that obtained by conventional techniques.

REFERENCES

[1] R. A. York and Z. B. Popovic, Eds., *Active and Quasi-Optical Arrays for Solid State Power Combining*. ser. in Microwave and Optical Engineering. New York: Wiley, 1997.

[2] H. Ito and E. Mosekilde *et al.*, "Bifurcation in a forced self-oscillatory system with spatial degrees of freedom," *Trans. Inst. Elect. Eng. Jpn. A*, vol. 113-A, no. 5, pp. 365–371, 1993.

[3] J. J. Lynch and R. A. York, "A mode locked array of coupled phase locked loops," *IEEE Microwave Guided Wave Lett.*, vol. 5, pp. 213–215, July 1995.

[4] R. J. Ram and R. Sporer *et al.*, "Chaos in microwave antenna arrays," in *1996 IEEE MTT-S Int. Microwave Symp. Dig.*. San Francisco, CA: IEEE, 1996.

[5] W. L. Ditto and M. L. Spano *et al.*, "Techniques for the control of chaos," *Physica D*, vol. 86, no. 1–2, pp. 198–211, 1995.

[6] C. A. Balanis, *Antenna Theory: Analysis and Design*. New York: Wiley, 1996.

[7] K. Wiesenfeld and P. Colet *et al.*, "Synchronization transitions in a disordered Josephson series array," *Phys. Rev. Lett.*, vol. 76, no. 3, pp. 404–407, 1996.

[8] K. Wiesenfeld and P. Colet *et al.*, "Frequency locking in Josephson arrays: Connection with the Kuramoto model," *Phys. Rev. E*, vol. 57, no. 2, pp. 1563–1569, 1998.

[9] D. D'Humieres and M. R. Beasley *et al.*, "Chaotic states and routes to chaos in the forced pendulum," *Phys. Rev. A*, vol. 26, no. 6, pp. 3483–3496, 1982.

[10] L. Jenshan and T. Itoh, "Active integrated antennas," *IEEE Trans. Microwave Theory Tech.*, vol. 42, pp. 2186–2194, Dec. 1994.

[11] J. F. Diouris and S. McLaughlin *et al.*, "Sensitivity analysis of the performance of a diversity receiver," in *1999 IEEE Int. Conf. Communications*. Piscataway, NJ, 1999.

[12] Y. Braiman, J. F. Lindner, and W. L. Ditto, "Taming spatiotemporal chaos with disorder," *Nature*, vol. 378, pp. 465–467, Nov. 1995.

[13] J. J. Lynch, H.-C. Chang, and R. A. York, "Coupled-oscillator arrays and scanning techniques," in *Active and Quasi-Optical Arrays for Solid-State Power Combining*, R. A. York and Z. B. Popovic, Eds. New York: Wiley, 1997, pp. 135–186.

[14] R. A. York, P. Liao, and J. J. Lynch, "Oscillator array dynamics with broadband N-port coupling networks," *IEEE Trans. Microwave Theory Tech.*, vol. 42, pp. 2040–2045, Nov. 1994.

[15] H. C. Chang, E. S. Shapiro, and R. A. York, "Influence of the oscillator equivalent circuit on the stable modes of parallel-coupled oscillators," *IEEE Trans. Microwave Theory Tech.*, vol. 45, pp. 1232–1239, Aug. 1997.

[16] S. H. Strogatz, "Exploring complex networks," *Nature*, vol. 410, pp. 268–276, Mar. 2001.

[17] L. Fabiny, P. Colet, R. Roy, and D. Lenstra, "Coherence and phase dynamics of spatially coupled solid-state lasers," *Phys. Rev. A*, vol. 47, no. 5, pp. 4287–4296, 1993.

[18] K. Wiesenfeld and J. W. Swift, "Averaged equations for Josephson junction series arrays," *Phys. Rev. E*, vol. 51, no. 2, pp. 1020–1025, 1995.

[19] R. A. York and T. Itoh, "Injection- and phase-locking techniques for beam control," *IEEE Trans. Microwave Theory Tech.*, vol. 46, pp. 1920–1929, Nov. 1998.

[20] A. H. Cohen, P. J. Holmes, and R. H. Rand, "The nature of the coupling between segmental oscillators of the lamprey spinal generator for locomotion: A mathematical model," *J. Math. Biol.*, vol. 13, pp. 345–369, 1982.

[21] I. Peterson, "Step in time: Exploring the mathematics of synchronously flashing fireflies," *Sci. News*, vol. 140, pp. 136–137, Aug. 1991.

[22] T. Heath, K. Wiesenfeld, and R. A. York, "Manipulated synchronization: Beam steering in phased arrays," *Int. J. Bif. Chaos*, vol. 10, no. 11, pp. 2619–2627, 2000.

[23] T. Heath, "Synchronization and phase dynamics of coupled oscillator," Ph.D. dissertation, Georgia Inst. Technology, Atlanta, 1999.

[24] R. J. Pogorzelski, P. F. Maccarini, and R. A. York, "A continuum model of the dynamics of coupled oscillator arrays for phase-shifterless beam scanning," *IEEE Trans. Microwave Theory Tech.*, vol. 47, Apr. 1999.

[25] R. J. Pogorzelski, "A two-dimensional coupled oscillator array," *IEEE Trans. Microwave Guided Wave Lett.*, vol. 10, pp. 478–480, Nov. 2000.

[26] A. Alexanian, H. C. Chang, and R. A. York, "Enhanced scanning range in coupled oscillator arrays utilizing frequency multipliers," in *1995 IEEE Antennas Propaga. Soc. Symp. Dig.*, Newport Beach, CA, pp. 1308–1310.

[27] T. Heath, "Difference pattern beam steering of coupled, nonlinear oscillator arrays," *IEEE Microwave Wireless Comp. Lett.*, submitted for publication.

[28] J.-H. Hwang and N.-H. Myung, "A new beam-scanning technique by controlling the coupling angle in a coupled oscillator array," *IEEE Microwave Guided Wave Lett.*, vol. 8, pp. 191–193, May 1998.

[29] G. V. Osipov and M. M. Suschik, "Synchronized clusters and multistability in arrays of oscillators with different natural frequencies," *Phys. Rev. E*, vol. 58, no. 6, pp. 7198–7207, 1998.

[30] T. W. Vadivasova, G. I. Strelkova, and V. S. Anischenko, "Phase-frequency synchronization in a chain of periodic oscillators and harmonic forcings," *Phys. Rev. E*, vol. 63, p. 036225, 2001.

[31] J. Guckenheimer, "Dynamics of the Van der Pol equation," *IEEE Trans. Circuits Syst.*, vol. CAS-27, pp. 983–989, Nov. 1980.

[32] D. W. Storti and R. H. Rand, "Dynamics of two strongly coupled Van der Pol oscillators," *Int. J. Non-Linear Mech.*, no. 3, pp. 143–152, 1982.

[33] H. G. Davies and D. Nandlall, "The response of a van der Pol oscillator to a modulated amplitude sinusoidal input," *J. Sound Vib.*, vol. 140, no. 3, pp. 499–512, 1990.

[34] C. A. Mead, *Analog VLSI and Neural Systems*. Reading, MA: Addison-Wesley, 1989.

[35] M. Mahowald and R. Douglas, "A silicon neuron," *Nature*, vol. 354, no. 6354, pp. 515–518, 1991.

[36] S. P. DeWeerth and G. N. Patel *et al.*, "Variable linear-range subthreshold OTA," *Electron. Lett.*, vol. 33, no. 15, pp. 1309–1311, 1997.

[37] C. A. Mead and T. Delbruck, "Scanners for visualizing activity of analog VLSI circuitry," *Anal. Int. Circuits Signal Process.*, vol. 1, no. 2, pp. 93–106, 1991.

[38] S. H. Strogatz, *Nonlinear Dynamics and Chaos: With Applications to Physics, Biology, Chemistry, and Engineering*. Reading, MA: Perseus, 1994.

Brian K. Meadows received the B.S. degree in physics from the University of California at Irvine in 1989 and the Ph.D. degree in physics from Georgia Institute of Technology, Atlanta, in 1998.

As Chief Scientist for Navigation and Timing for the U.S. Navy, he oversees basic and applied research in these areas. Concurrently, he leads the Applied Chaos and Dynamics research group at the Space and Naval Warfare System Center, San Diego. In addition, he is an engineering officer in the Naval Reserve.

Ted H. Heath received the B.S. and Ph.D. degrees in physics from Georgia Institute of Technology (Georgia Tech), Atlanta, in 1993 and 1999, respectively.

He is currently a Research Scientist II in the Sensors and Electromagnetic Applications division of the Georgia Tech Research Institute.

Joseph D. Neff received the B.A. degree from the College of Wooster in 1993 and the Ph.D. degree in physics from the Georgia Institute of Technology, Atlanta, in 2000.

He currently works at SPAWAR Systems Center, San Diego, CA, in the nonlinear dynamics group. His current areas of interests include stochastic resonance and signal transduction in biological and engineered systems, and nonlinear dynamical arrays of coupled oscillators.

Edgar A. Brown received the B.S. and M.S. degrees in electronics engineering from Universidad Simm Bolvar, Venezuela, in 1987 and 1992, respectively, and the M.S. degree in applied math from the Georgia Institute of Technology, Atlanta, in 1999. He is currently working toward the Ph.D. degree in electrical and computer engineering at the same univeristy.

He is currently a Research Engineer with the Laboratory for Neuroengineering, Georgia Institute of Technology.

David W. Fogliatti received the B.S. degree in physics from the University of California at Los Angeles in 1999.

He is currently working at SPAWAR Systems Center, San Diego, CA, in the nonlinear dynamics group exploring application of nonlinear dynamics to communication and navigation systems.

Michael Gabbay received the B.A. degree in physics from Cornell University, Ithaca, NY, in 1985 and the Ph.D. degree in physics from the University of Chicago in 1997.

He is currently a Principal Scientist with Information Systems Laboratories, Inc., San Diego, CA. His research interests are in nonlinear dynamics, pattern formation and recognition, and signal and image processing.

Visarath In received the B.S. degree in physics and mathematics from Jacksonville University, Jacksonville, FL, in 1991, and the Ph.D. in physics in the field of experimental nonlinear dynamics from Georgia Institute of Technology, Atlanta, in 1996.

Since then, he has worked at NSWC, Carderock Division and now he is working at SPAWAR Systems Center, San Diego, CA.

Paul Hasler (Member, IEEE) received the B.S.E. and M.S. degrees in electrical engineering from Arizona State University, Tempe, in 1991 and the Ph.D. degree in computation and neural systems from the California Institute of Technology, Pasadena, in 1997.

He is currently an Assistant Professor at the School of Electrical and Computer Engineering, Georgia Institute of Technology, Atlanta.

Stephen P. Deweerth (Member, IEEE) received the B.A. degree in mathematics and chemistry from Wartburg College, Waverly, IA, in 1985, and the M.S. degree in computer science and the Ph.D. degree in computation and neural systems from the California Institute of Technology.

He is currently an Associate Professor at the Emory Department of Biomedical Engineering, Georgia Institute of Technology, Atlanta.

William L. Ditto received the B.S. degree in physics from the University of California at Los Angeles in 1980, and the Ph.D. degree in physics from Clemson University in 1988.

He is currently the Chair of the Department of Biomedical Engineering, University of Florida, Gainesville.